

## Article

# LiGd<sub>x</sub>Y<sub>1-x</sub>F<sub>4</sub> and LiGdF<sub>4</sub>:Eu<sup>3+</sup> Microparticles as Potential Materials for Optical Temperature Sensing

Ekaterina I. Oleynikova <sup>1,\*</sup>, Oleg A. Morozov <sup>1,2</sup>, Stella L. Korableva <sup>1</sup> and Maksim S. Pudovkin <sup>1,\*</sup><sup>1</sup> Institute of Physics, Kazan Federal University, 18 Kremlyovskaya str, 420008 Kazan, Russia<sup>2</sup> Zavoisky Physical-Technical Institute, FRC Kazan Scientific Center of RAS, Sibirsky Trakt str. 10, 420029 Kazan, Russia

\* Correspondence: kate15-05@mail.ru (E.I.O.); jaz7778@list.ru (M.S.P.)

**Abstract:** In this work, the physical characterization of LiGd<sub>x</sub>Y<sub>1-x</sub>F<sub>4</sub> (x = 0.05, 0.3, 0.7, and 1.0) and LiGdF<sub>4</sub>:Eu<sup>3+</sup> microparticles was performed. The distribution coefficient of LiGd<sub>x</sub>Y<sub>1-x</sub>F<sub>4</sub> (x = 0.05) was determined for the first time (0.84). Based on kinetic characterization data, the LiGdF<sub>4</sub> sample was chosen for further Eu<sup>3+</sup> doping (0.1 and 1.0 at.%). For the LiGdF<sub>4</sub>:Eu<sup>3+</sup> sample, Eu<sup>3+</sup> emission was clearly observed under the excitation of Gd<sup>3+</sup>. This fact indicates an effective energy transfer from Gd<sup>3+</sup> to Eu<sup>3+</sup>. The temperature-dependent spectral characterization of the LiGdF<sub>4</sub>:Eu<sup>3+</sup> (1.0%) sample revealed that in the 30–250 K temperature range, a broad emission peak is evidenced. Its intensity sharply increases with the temperature decrease. We made a suggestion that this phenomenon is related to the irradiation-induced defects. The integrated luminescence intensity ratio of this broad peak and the Eu<sup>3+</sup> emission were taken as temperature-dependent parameters. The sensitivity values are very competitive, and the first maximum occurs at 174 K (3.18%/K). The kinetic characteristics of both Gd<sup>3+</sup> and Eu<sup>3+</sup> did not demonstrate a notable temperature dependence. The LiGdF<sub>4</sub>:Eu<sup>3+</sup> sample showed the possibility of being used as an optical temperature sensor, operating in the cryogenic temperature range.

**Keywords:** LiGdF<sub>4</sub>; Eu<sup>3+</sup>; LiGdF<sub>4</sub>:Eu<sup>3+</sup>; luminescence thermometry; cryogenic temperature sensors; distribution coefficient



**Citation:** Oleynikova, E.I.; Morozov, O.A.; Korableva, S.L.; Pudovkin, M.S. LiGd<sub>x</sub>Y<sub>1-x</sub>F<sub>4</sub> and LiGdF<sub>4</sub>:Eu<sup>3+</sup> Microparticles as Potential Materials for Optical Temperature Sensing. *Ceramics* **2024**, *7*, 276–290. <https://doi.org/10.3390/ceramics7010018>

Academic Editor: Francesco Scotognella

Received: 19 September 2023

Revised: 1 November 2023

Accepted: 1 February 2024

Published: 23 February 2024



**Copyright:** © 2024 by the authors. Licensee MDPI, Basel, Switzerland. This article is an open access article distributed under the terms and conditions of the Creative Commons Attribution (CC BY) license (<https://creativecommons.org/licenses/by/4.0/>).

## 1. Introduction

Rare-earth-doped and un-doped nano- and microsized LiREF<sub>4</sub> (RE = rare-earth ions) crystals are considered highly promising materials for quantum electronics, solar cells, optical temperature sensing, and bioimaging [1–8]. The doping—rare-earth ions—are characterized by a partially filled 4f shell that is effectively shielded by 5 s<sup>2</sup> and 5 p<sup>6</sup> orbitals. Therefore, the spectrum of rare-earth-doped luminescent materials consists of narrow and intense luminescence peaks. Compared with other luminescent materials (e.g., organic dye, quantum dots, etc.), rare-earth-doped luminescent materials have many advantages, such as a sharp emission and long luminescence lifetime, good photochemical and thermal stability [9], and a lack of photobleaching, etc. [10]. The luminescent properties of RE-doped fluoride materials are mainly influenced by the host matrix, as well as the doping ions. Hence, the optimal host–doping ion combinations are necessary for efficient luminescence processes. Among the RE ions, the Eu<sup>3+</sup>/Gd<sup>3+</sup> ion pair seems to be promising and is less studied. Indeed, the Gd<sup>3+</sup> ion shows intense luminescence due to the f–f transitions in numerous hosts, demonstrating a strong emission in the 290–312 nm range [11]. The luminescence and laser generation in this spectral range is highly demanded in the treatment of skin diseases, such as vitiligo and psoriasis [12]. In turn, Eu<sup>3+</sup> itself has a strong temperature sensitivity in relation to its spectral–kinetic characteristics [13]. In the case of the Gd<sup>3+</sup>/Eu<sup>3+</sup> ion pair, recent studies have demonstrated a significant enhancement of Eu<sup>3+</sup> luminescence under UV Gd<sup>3+</sup> excitation due to the Gd<sup>3+</sup> → Eu<sup>3+</sup> energy transfer process. Moreover, materials doped with Gd<sup>3+</sup> and Eu<sup>3+</sup> have been proposed as promising materials for red

lasers [2,4,14]. However, the  $Gd^{3+}/Eu^{3+}$  ion pair is significantly less studied in terms of its temperature-dependent spectral–kinetic characterization, compared to such widespread ion pairs as  $Nd^{3+}/Yb^{3+}$  [15],  $Er^{3+}/Yb^{3+}$  [16],  $Eu^{3+}/Tb^{3+}$  [17,18], and  $Ce^{3+}/Yb^{3+}$  [19]. The  $LiYF_4$  matrix was chosen as the host, which decreases the non-radiative relaxation due to the low phonon energy of the host matrix. The  $Gd^{3+}/Eu^{3+}$  combination was used as a donor/acceptor pair due to the presence of phonon-assisted energy transfer between them, which leads to potential temperature-dependent spectral–kinetic characteristics of the system. In turn,  $Eu^{3+}$  demonstrates luminescence in the visible part of the spectrum. The ability to convert UV into visible light is highly required due to the increasing need for silicon solar cell efficiency [14]. For these reasons, a thorough and detailed investigation of the spectral–kinetic characteristics of  $LiGd_xY_{1-x}F_4:Eu^{3+}$  is very useful for the abovementioned applications. The main novelty of this work is that we characterize a set of samples ( $LiGd_xY_{1-x}F_4$  ( $x = 0.05, 0.3, 0.7, \text{ and } 1.0$ )) in order to choose a suitable one for  $Eu^{3+}$  doping. Additionally, the distribution coefficient of  $LiGd_xY_{1-x}F_4$  ( $x = 0.05$ ) is determined for the first time. The crystals with different  $Gd^{3+}$  concentrations were successfully prepared using the Bridgman–Stockbarger method and, then, they were mechanically milled into microparticles. The structural and photoluminescence properties were investigated. The  $LiGd_xY_{1-x}F_4:Eu^{3+}$  particles showed efficient energy transfer and high temperature sensitivity over a wide temperature range. This observation allows them to be used as coatings for solar panels, as well as luminescent temperature sensors. The objective of this study was to estimate the possibility of using  $LiY_xGd_{1-x}F_4$  and  $Eu^{3+}:LiGdF_4$  phosphors in optical temperature sensing. The tasks were the synthesis and the spectral–kinetic characterization of  $Gd^{3+}$  in  $LiY_xGd_{1-x}F_4$  in order to choose an appropriate ratio of  $Gd^{3+}$  and  $Y^{3+}$  ions, and the spectral–kinetic characterization of  $Eu^{3+}$  in  $Eu^{3+}:LiY_xGd_{1-x}F_4$  in the 10–320 K temperature range.

## 2. Materials and Methods

In this work, we investigated  $LiGd_xY_{1-x}F_4$  ( $x = 0.05, 0.3, 0.5, 0.7, \text{ and } 1.0$ ) and  $Eu^{3+}$  (0.1 and 1.0 at.%) $:LiGdF_4$  crystals. Optically perfect, single  $LiGd_xY_{1-x}F_4$  crystals were grown using the Bridgman–Stockbarger technique, using a growth furnace with a specially designed heating unit. The comprehensive crystal growth procedure is described in our previous work [7]. To record the absorption spectra, a DFS-452 spectrograph (1200 ruling/mm lattice, 0.5–0.2 nm/mm inverse linear dispersion, 120,000 theoretical resolution of the spectrograph, spectral resolution 0.3 nm) and a broadband light source (deuterium lamp) were used. Elements analysis was carried out by means of energy-dispersive X-ray spectroscopy (EDX), using a scanning electron microscope, Dimension FastScan (Santa Barbara, CA, USA). The concentration of both  $Eu^{3+}$  and  $Gd^{3+}$  ions was calculated as a mass proportion of the  $EuF_3$  and  $GdF_3$  starting materials in the melt. The phase composition of the particles was confirmed by means of the X-ray diffraction method (XRD), using a Bruker D8 ADVANCE X-ray diffractometer (Cu  $K_\alpha$  radiation,  $\lambda = 0.154$  nm). The XRD simulation was carried out using VESTA software, version 3 (Ibaraki, Japan). The luminescence spectra were recorded by a CCD spectrometer StellarNet, (Tampa, FL, USA) (~1.0–2.0 nm spectral resolution). The optical excitation of the samples was performed using a LOTIS TII tunable laser, LT-2211A ( $\lambda_{ex} (Gd^{3+}) = 274$  nm,  $\tau = 10$  ns,  $\nu = 10$  Hz). The experiments were performed in the 10–320 K temperature range via the so-called “cold finger” method. The temperature control was carried out using a thermostatic cooler “CRYO industries”, which had a LakeShore Model 325 (Westerville, OH, USA) temperature controller. The luminescence decay time curves were recorded using a Bordo 211A digital oscilloscope (10 bit and 200 MHz bandwidth), an MDR-3 monochromator, and a PEM-62 photomultiplier (working spectral range ~ 600–1200 nm). All the calculations were carried out using the Origin Pro 9.0 software.

### 3. Results

#### 3.1. XRD Characterization of the $\text{LiGd}_x\text{Y}_{1-x}\text{F}_4$ Samples

The phase composition of the  $\text{LiGd}_x\text{Y}_{1-x}\text{F}_4$  ( $X = 0.05, 0.3, 0.7,$  and  $1.0$ ) samples was confirmed via XRD method. The XRD patterns of the  $\text{LiGd}_x\text{Y}_{1-x}\text{F}_4$  samples, the simulation of  $\text{LiGdF}_4$ , and JCPDS are presented in Figure 1.

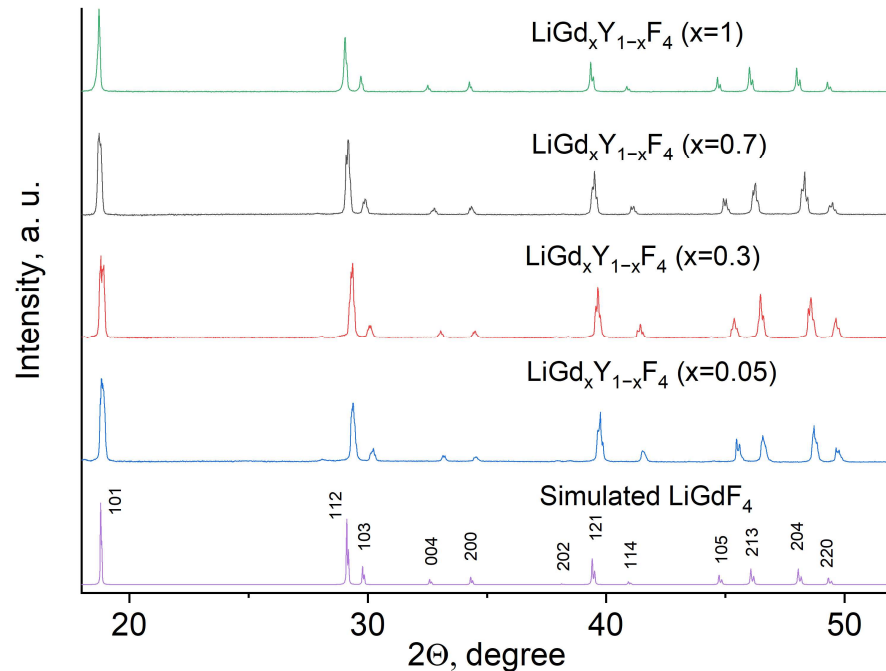


**Figure 1.** The XRD patterns, simulation, and JCPDS of the  $\text{LiGd}_x\text{Y}_{1-x}\text{F}_4$  ( $X = 0.05, 0.3, 0.7,$  and  $1.0$ ) samples.

The XRD patterns correspond to the trigonal structure of both  $\text{LiYF}_4$  and  $\text{LiGdF}_4$  matrices. The well-defined peaks, the absence of impurity peaks, and the absence of amorphous phases are seen. The experimental XRD patterns agree with the reference patterns from the VESTA software, version 3. They also agree with JCPDS No. 027–1236 [20]. According to the literature data, the lattice parameters of  $\text{LiGdF}_4$  are  $a = 0.5235$  (1) nm,  $c = 1.1019$  (2) nm [21]. In its turn, the lattice parameters of  $\text{LiYF}_4$  are  $a = 0.5164$  (1) nm,  $c = 1.074$  (2) nm [22]. The XRD peaks also slightly shift toward higher angles with the decrease in  $\text{Gd}^{3+}$  content, expressing the Bragg law. The calculated lattice parameters are in agreement with the above-mentioned values and gradually increase with the increase in  $\text{Gd}^{3+}$  content (Table S1, Supplementary Materials).

#### 3.2. Spectral–Kinetic Characterization of the $\text{LiGd}_x\text{Y}_{1-x}\text{F}_4$ Samples

For this work, optically perfect crystals (65 mm in length) were grown. Since the undoped  $\text{LiGd}_x\text{Y}_{1-x}\text{F}_4$  ( $X = 0.05, 0.3, 0.5, 0.7,$  and  $1.0$ ) crystals are insufficiently studied, there is no information in the literature about the distribution coefficient of  $\text{Gd}^{3+}$ ; therefore, we measured the distribution coefficient of the  $\text{Gd}^{3+}$  ions in the  $\text{LiYF}_4$  matrix. The information concerning the distribution coefficient of  $\text{Gd}^{3+}$  is very important for quantum electronics and laser technologies [23]. For this purpose, the  $\text{LiYF}_4:\text{Gd}^{3+}$  (5 at.%) was prepared according to Figure 2a. The setup is shown in Figure 2b. The photo of the sample is represented in Figure S1 (Supplementary Materials).

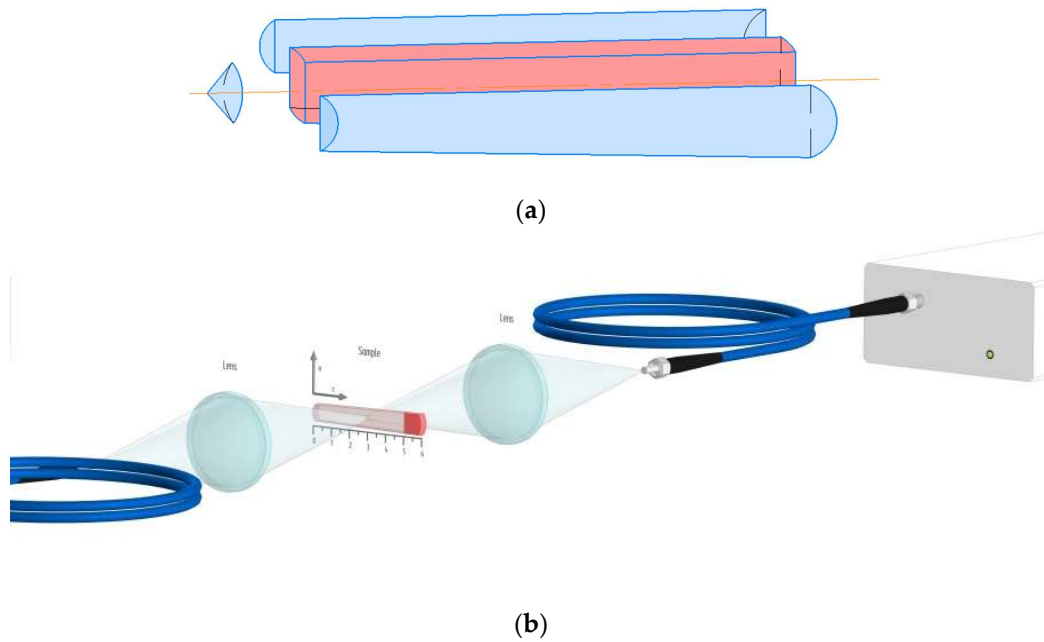


**Figure 2.** (a) Preparation of the crystal for the experiment; (b) schematic representation of the experimental set-up.

For the crystal growth procedure by the Bridgman method for low crystal pulling rates (a few millimeters per hour), it can be assumed that the solution is completely mixed in the liquid. Therefore, to characterize the impurity distribution in the grown crystal, the Scheil equation can be used [24]:

$$C(x) = C_0 k (1 - x)^{k-1} \quad (1)$$

where  $C_0$  is the concentration of the starting material,  $x$ —volume fraction of solid, and  $k$ —distribution coefficient. The integral absorbance  $A$  is proportional to the concentration [25] of  $\text{Gd}^{3+}$  ions in the crystal. Therefore, the Scheil equation can be rewritten as follows:

$$A_s = k A_0 (1 - x)^{k-1} \quad (2)$$

Thus, to determine the partition coefficient, we recorded the absorption spectra of  $\text{Gd}^{3+}$  ions in the 270–280 nm spectral range (Figure S2, Supplementary Materials). The absorption spectra were recorded along the crystal at points with an increment of 3 mm. Next, the integral absorbance was calculated in the 270–280 nm wavelength range and the dependence of the integral absorbance in arbitrary units on the solidified fraction was plotted. Fitting the graph according to the Scheil equation gives the distribution coefficient and integral absorbance  $A_0$  for the initial concentration  $C_0$ . The initial concentration is the concentration of  $\text{Gd}^{3+}$  that we put into the mixture at the beginning of growth. It is equal to 5%. Taking into account the initial concentration and the corresponding integral absorption, we can recalculate the integral absorption data into concentration at the corresponding points. The data obtained in this way is presented in Figure 3. The energy-dispersive X-ray spectroscopy (EDX) confirms the obtained  $\text{Gd}^{3+}$  distribution. To obtain the standard deviations, we performed EDX measurements from five different parts of the crystal cap, middle part, and spout.

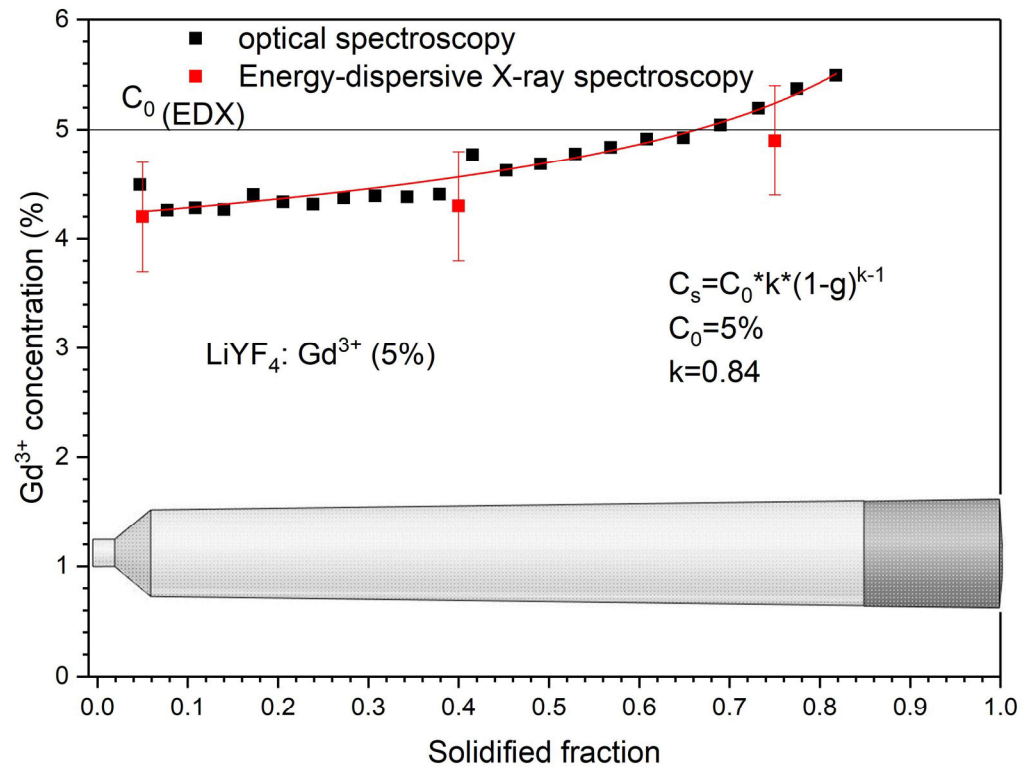


**Figure 3.** The distribution of Gd<sup>3+</sup> ions in LiGd<sub>x</sub>Y<sub>1-x</sub>F<sub>4</sub> (x = 0.05) crystal volume. Energy-dispersive X-ray spectroscopy (EDX) confirms the obtained Gd<sup>3+</sup> distribution.

The energy level diagram and excitation scheme of the Gd<sup>3+</sup>/Eu<sup>3+</sup> system are represented in Figure 4. The Gd<sup>3+</sup>—Eu<sup>3+</sup> energy transfer process will be discussed below.

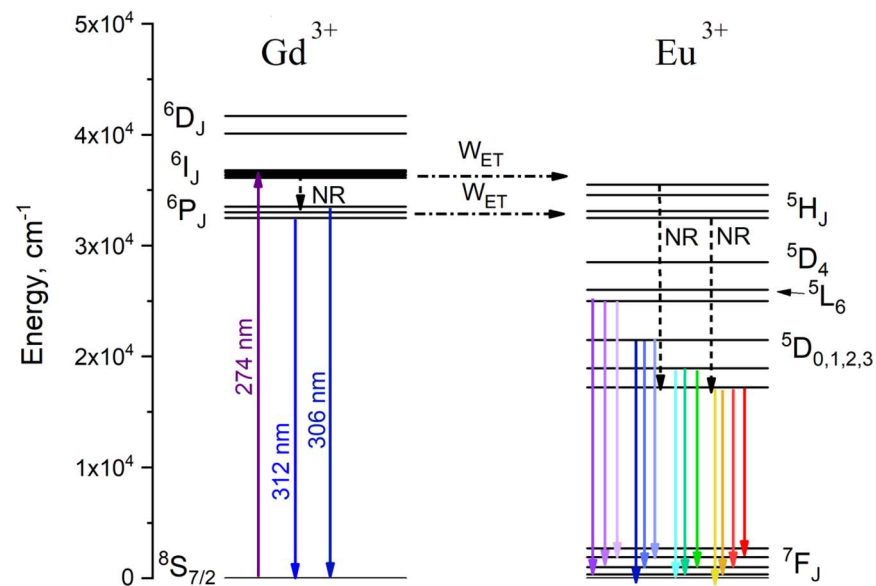


**Figure 4.** Energy level diagram and excitation scheme of Gd<sup>3+</sup>/Eu<sup>3+</sup> ion pair.  $\lambda_{ex} = 274$  nm corresponds to  $^8S_{7/2} \rightarrow ^6I_J$  absorption band of Gd<sup>3+</sup>. The dotted arrows explain the energy transfer ( $W_{ET}$ ) from Gd<sup>3+</sup> to Eu<sup>3+</sup>

The 274 nm excitation wavelength corresponds to the  $^8S_{7/2} \rightarrow ^6I_J$  absorption band of Gd<sup>3+</sup>. The luminescence decay times of  $^6P_{7/2} \rightarrow ^8S_{7/2}$  (at 312 nm) as functions of temperature are represented in Figure 5. The luminescence decay curves detected at different temperatures are represented in Figure S3 (Supplementary Materials).

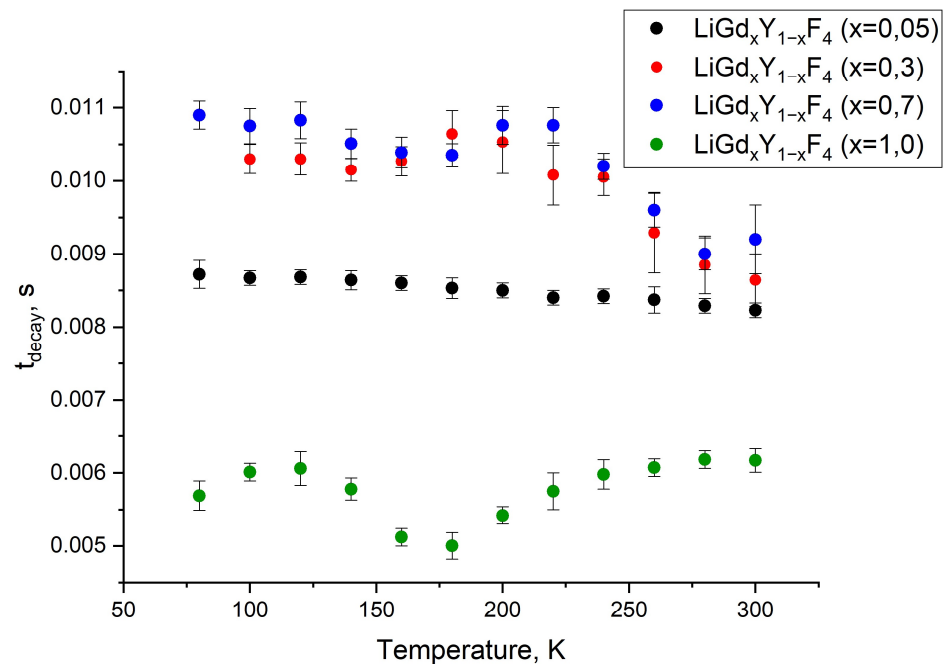


**Figure 5.** The luminescence decay time ( $t_{\text{decay}}$ ) of the  $\text{LiGd}_x\text{Y}_{1-x}\text{F}_4$  samples ( $x = 0.05; 0.3; 0.7$  and  $1.0$ ) at a wavelength of  $312 \text{ nm}$  ( ${}^6\text{P}_{7/2} \rightarrow {}^8\text{S}_{7/2}$ ) in the  $100\text{--}300 \text{ K}$  temperature range.

There are very few papers devoted to the concentration quenching of  $\text{Gd}^{3+}$  ions, especially in fluoride hosts (single  $\text{Gd}^{3+}$ -doped systems). The difference in decay times for  $\text{LiGd}_{0.05}\text{Y}_{0.95}\text{F}_4$  and both  $\text{LiGd}_{0.3}\text{Y}_{0.7}\text{F}_4$  and  $\text{LiGd}_{0.7}\text{Y}_{0.3}\text{F}_4$  can be explained by the fact that there can be reabsorption of the luminescence that leads to the increase in the lifetime of the excited state. In more detail, we found in [26] that at  $300 \text{ K}$  the decay rate of  ${}^6\text{P}_{7/2}$  ( $\text{Gd}^{3+}$ ) in  $\text{LiYF}_4\text{-}1\%\text{Gd}^{3+}$  is equal to  $115 \text{ (s}^{-1}\text{)}$ ; hence, the decay time can be calculated as the inverse value =  $8.7 \text{ ms}$ . In our  $\text{Gd}^{3+}$  (5%):  $\text{LiYF}_4$  sample, the decay time is also around  $8.5 \text{ ms}$ . It can be suggested that at lower concentrations, the decay time of  ${}^6\text{P}_{7/2}$  ( $\text{Gd}^{3+}$ ) is around  $8.5 \text{ ms}$ . With higher concentrations, the contribution of reabsorption is higher than the contribution of concentration quenching. This leads to an increase in the decay time. Thus it can be suggested that, for the  $\text{LiGdF}_4$  sample, the contribution of concentration quenching is predominant, and a decrease in the decay time is observed. It can be seen that for the  $\text{LiGd}_x\text{Y}_{1-x}\text{F}_4$  samples ( $x = 0.05; 0.3$  and  $0.7$ ), the luminescence decay time slightly shortens with the temperature increase. This expected tendency can be explained by the multiphonon relaxation on defects. Indeed, its efficiency decreases with the temperature increase. In its turn, for the  $\text{LiGdF}_4$  sample, the opposite trend is observed: an increase in the luminescence decay time with the increase in the temperature, starting from  $180 \text{ K}$ . For this sample, the reabsorption of the luminescence plays a more significant role. The reabsorption efficiency can rise with the temperature increase due to the broadening of the absorption bands. This is the same phenomenon we earlier observed for  $\text{Yb}^{3+}$  ions [27]. However, the observed phenomena require additional investigation. After the kinetic characterization of the  $\text{LiGd}_x\text{Y}_{1-x}\text{F}_4$  samples, the  $\text{LiGdF}_4$  one was selected for further doping with  $\text{Eu}^{3+}$  because there are at least two temperature-dependent processes: multiphonon relaxation on defects and reabsorption of the luminescence. It is known that to obtain a higher temperature sensitivity of phosphors, as many temperature-dependent processes as possible are needed, which can eventually strengthen each other, resulting in higher temperature sensitivity. To avoid concentration quenching, the  $0.1$  and  $1.0$  at.% concentrations of  $\text{Eu}^{3+}$  were chosen. Room-temperature luminescence spectra of the  $\text{LiGdF}_4\text{:Eu}^{3+}$  ( $0.1$  (a) and  $1.0$  at.% (b)) sample under  $\text{Gd}^{3+}$  excitation ( ${}^8\text{S}_{7/2} \rightarrow {}^6\text{P}_j$  absorption band,  $\lambda_{\text{ex}} = 274 \text{ nm}$ ) are represented in Figure 6a,b, respectively.

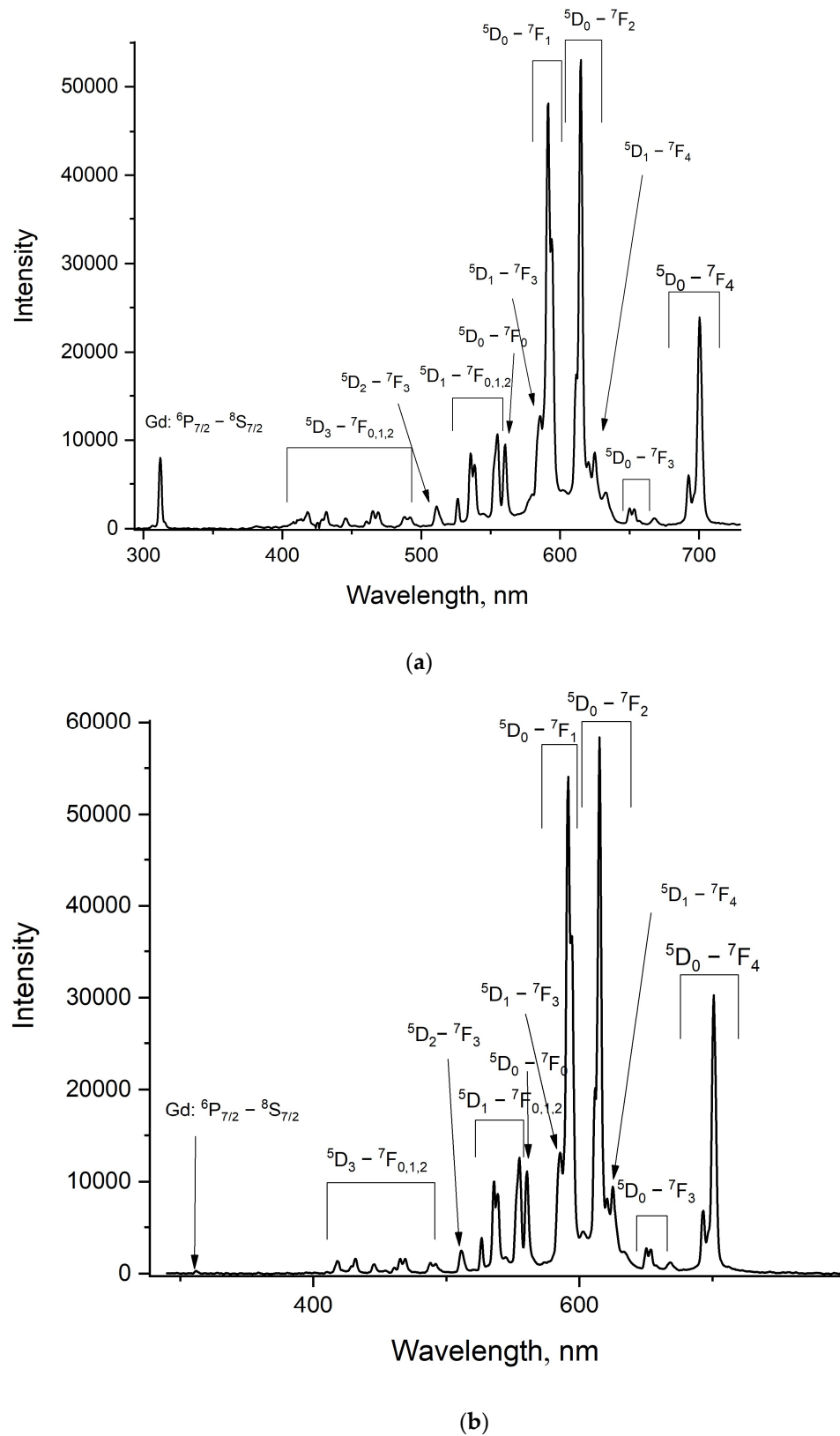


**Figure 6.** Room-temperature luminescence spectrum of the LiGdF<sub>4</sub>:Eu<sup>3+</sup> (0.1 (a) and 1.0% (b)) sample under the Gd<sup>3+</sup> excitation ( $\lambda_{ex} = 274$  nm,  $^8S_{7/2} \rightarrow ^6P_j$  absorption band).

It can be seen that for the LiGdF<sub>4</sub>:Eu<sup>3+</sup> (0.1%) sample, the luminescence peaks of both Gd<sup>3+</sup> and Eu<sup>3+</sup> doping ions are observed. To exclude the possibility of the direct excitation of Eu<sup>3+</sup> under 274 nm, we carried out the same experiment for LiYF<sub>4</sub>:Eu<sup>3+</sup>, where the

LiYF<sub>4</sub> host does not absorb this wavelength (274 nm). The pictures of both LiGdF<sub>4</sub>:Eu<sup>3+</sup> (0.1%) and LiYF<sub>4</sub>:Eu<sup>3+</sup> (0.1%) powders under 274 nm excitation are represented in Figure S4. For LiGdF<sub>4</sub>:Eu<sup>3+</sup> (0.1%), the characteristic red luminescence of Eu<sup>3+</sup> is clearly observed. LiYF<sub>4</sub>:Eu<sup>3+</sup> (0.1%) does not show emission. According to the literature data, the energy transfer from Gd<sup>3+</sup> to Eu<sup>3+</sup> occurs via quantum cutting [28] and energy transfer between suitable energy levels of Gd<sup>3+</sup> and Eu<sup>3+</sup> [29,30]. Quantum cutting can be described at the Gd<sup>3+</sup> excitation ( $\lambda_{\text{ex}} = 202 \text{ nm}$  (<sup>8</sup>S<sub>7/2</sub>—<sup>6</sup>G<sub>J</sub> absorption band of Gd<sup>3+</sup>)) as “cuts” into the excitation of the <sup>5</sup>D<sub>0</sub> level of Eu<sup>3+</sup> and <sup>6</sup>P<sub>J</sub> level of Gd<sup>3+</sup>. This process is possible only for the above-mentioned excitation scheme ( $\lambda_{\text{ex}} = 202 \text{ nm}$ ). In the present work, such quantum cutting is impossible. The energy transfer from Gd<sup>3+</sup> to Eu<sup>3+</sup> occurs via <sup>6</sup>I<sub>J</sub> (Gd<sup>3+</sup>)—<sup>5</sup>F<sub>J</sub>, <sup>5</sup>I<sub>J</sub> (Eu<sup>3+</sup>) and <sup>6</sup>P<sub>J</sub>—(Gd<sup>3+</sup>)—<sup>5</sup>F<sub>J</sub>, <sup>5</sup>I<sub>J</sub> (Eu<sup>3+</sup>). Gd<sup>3+</sup> ions can be optically excited at 274 nm (<sup>8</sup>S<sub>7/2</sub>—<sup>6</sup>I<sub>J</sub>). Then, the <sup>6</sup>I<sub>J</sub> states can decay non-radiatively, populating <sup>6</sup>P<sub>J</sub> excited states. The excitation energy can be transferred to the <sup>5</sup>H<sub>J</sub> states of Eu<sup>3+</sup>, following the non-radiative transition to the lower <sup>5</sup>D<sub>J</sub>. The lowest <sup>6</sup>P<sub>J</sub> (J = 7/2) of Gd<sup>3+</sup> has an energy of around 32,000 cm<sup>-1</sup> in LiGdF<sub>4</sub> [31]. In its turn, the highest <sup>5</sup>D<sub>J</sub> (J = 4) state of Eu<sup>3+</sup> has an energy of around 29,000 cm<sup>-1</sup> [32]. The highest phonon energy for LiGdF<sub>4</sub> is around 570 cm<sup>-1</sup> [33,34]. It required around five phonons to “bridge” the <sup>6</sup>P<sub>7/2</sub>—<sup>5</sup>D<sub>4</sub> energy gap. In the case of <sup>6</sup>I<sub>J</sub> (Gd<sup>3+</sup>)—<sup>5</sup>F<sub>J</sub>, <sup>5</sup>I<sub>J</sub> (Eu<sup>3+</sup>) energy transfer, there is also an energy gap of the same order. It can be suggested that this energy transfer is phonon-assisted at our excitation conditions. This energy transfer leads to the intense Eu<sup>3+</sup> emission under Gd<sup>3+</sup> excitation. In its turn, the LiGdF<sub>4</sub>:Eu<sup>3+</sup> (1.0%) sample demonstrates negligible Gd<sup>3+</sup> luminescence. It can be suggested that higher Eu<sup>3+</sup> concentrations quench Gd<sup>3+</sup> more efficiently. Due to the efficient energy transfer from Gd<sup>3+</sup> (donor) to Eu<sup>3+</sup> (acceptor), this material can be used as coatings for silicon-based solar cells [35]. Indeed, for these solar panels, it is very important to convert UV radiation into visible light and IR, since there are intense absorption bands of silicon in the visible and IR ranges.

### 3.3. Spectral Characterization of the LiGdF<sub>4</sub>:Eu<sup>3+</sup> (1 at.%)

The LiGdF<sub>4</sub>:Eu<sup>3+</sup> (1 at.%) luminescence spectra were recorded in the 30–320 K temperature range (Figure 7). We immediately noticed broadband emission peaks in the visible spectral region (~350–650 nm) and a simultaneous decrease in the intensity of Eu<sup>3+</sup> emission at low temperatures: the same phenomenon we earlier observed in our previous work for Nd<sup>3+</sup>, Yb<sup>3+</sup>: YF<sub>3</sub> crystalline particles [36].

Particularly, the presence of this broad emission can be explained by several mechanisms. In the work of [37], the broad excitonic emission is observed for LiYF<sub>4</sub> (the same crystal structure as LiGdF<sub>4</sub>) under X-ray excitation at 4.2 K. These excitons are of the type  $F_2^{2-}$ . However, this emission in the 200–400 K spectral range centered at 300 nm, unlike the obtained results (Figure 7). Moreover, the excitonic emission is thermally quenched at  $T > 100 \text{ K}$ . Here, we observe a broad emission at higher temperatures [38]. The second mechanism is related to the presence of oxygen impurities which are considered the most common impurity for fluorides. There are also fluorine vacancies (V<sub>F</sub>): in this case, fluoride matrices where the fluorine ion is substituted by oxygen. The absorption band of these impurities is in the 250–300 nm range. Our excitation wavelength (274 nm) is almost at the center of the absorption band [39]. We found at least two consequences of the presence of the oxygen impurities (O<sub>F</sub>). The first is the O<sub>F</sub>—RE<sup>3+</sup> complex [39] and the second is the O<sub>F</sub>—VF—RE<sup>3+</sup> one [40]. Under UV excitation, both doping ions and the above-mentioned complexes are excited following the emission or non-radiative transitions. It can be suggested that the O<sub>F</sub>—RE<sup>3+</sup> and O<sub>F</sub>—VF—RE<sup>3+</sup> complexes have an intricate energy level structure that provides broad-band emission. At low temperatures, the energy transfer from the complex to RE is hindered and we observe the broad emission of the complexes. The energy transfer probability increases with the rise in the temperature, which leads to the decrease in the complex emission intensity and the increase in RE emission. This hypothesis requires additional investigation.

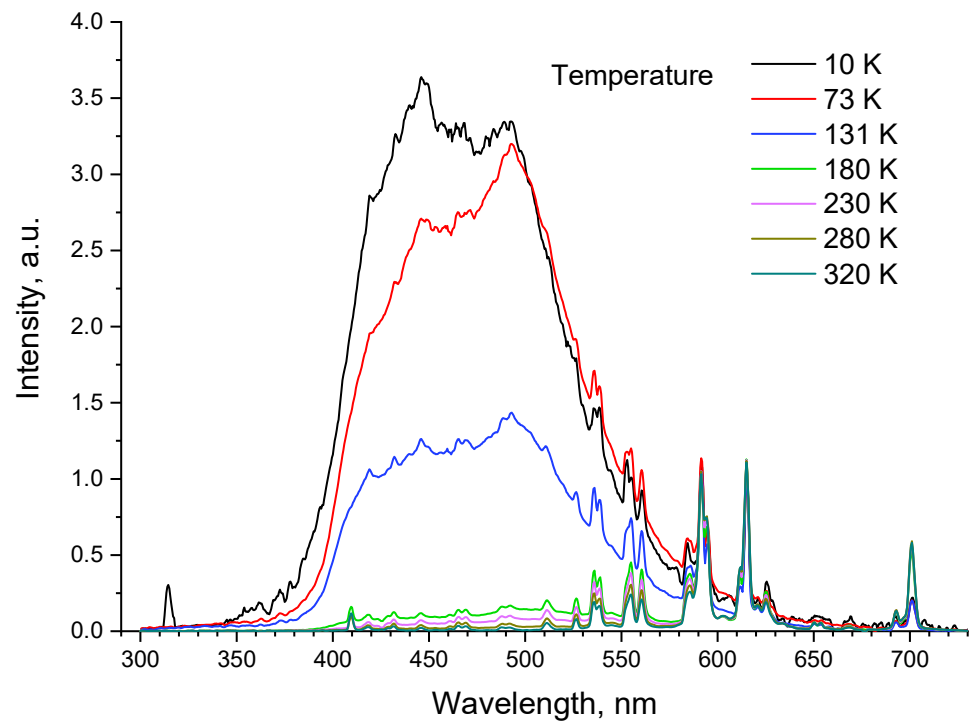


Figure 7. Luminescence spectrum of LiGdF<sub>4</sub>:Eu<sup>3+</sup> (1.0%) in the 10–290 K temperature range.

Having used the baseline function in OriginPro 9.0 software, we separated the luminescence spectrum of Eu<sup>3+</sup> and the defects. The luminescence intensity ratio (*LIR*) between the luminescence of the defects and Eu<sup>3+</sup> was taken as a temperature-dependent parameter. The *LIR* curves as functions of temperature are represented in Figure 8.

$$LIR = \frac{I_{defects}}{I_{Eu^{3+}}} \tag{3}$$

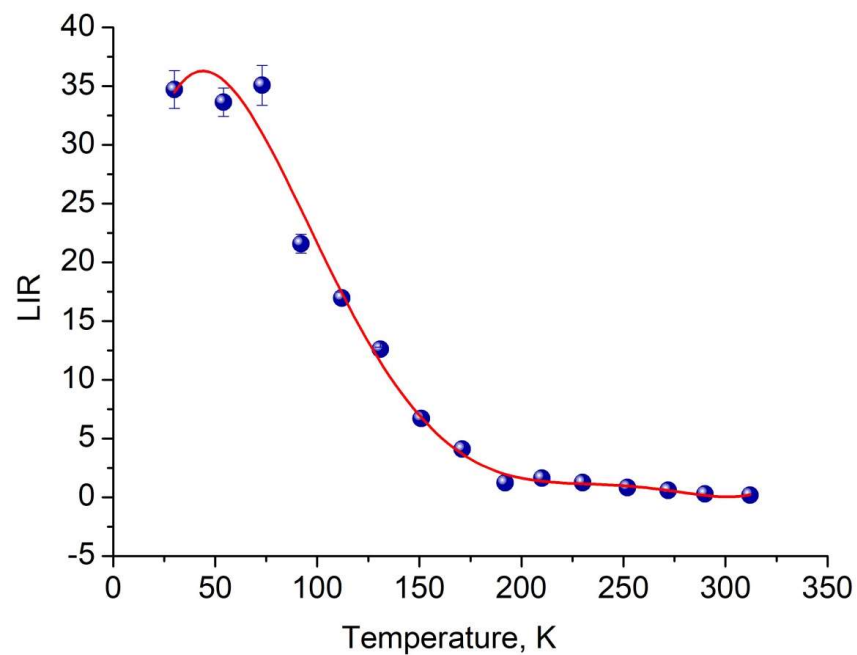
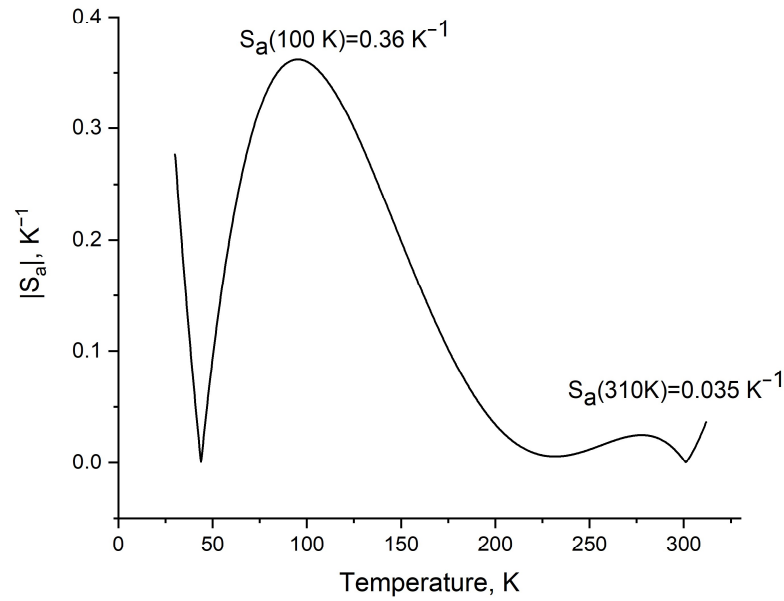


Figure 8. *LIR* as a function of temperature. The approximation function is determined as  $LIR = 9.8 + 1.412 \cdot T - 2.4 \cdot 10^{-2} \cdot T^2 + 1.5 \cdot 10^{-4} \cdot T^3 - 4.0 \cdot 10^{-7} \cdot T^4 + 4.0 \cdot 10^{-10} \cdot T^5$ .

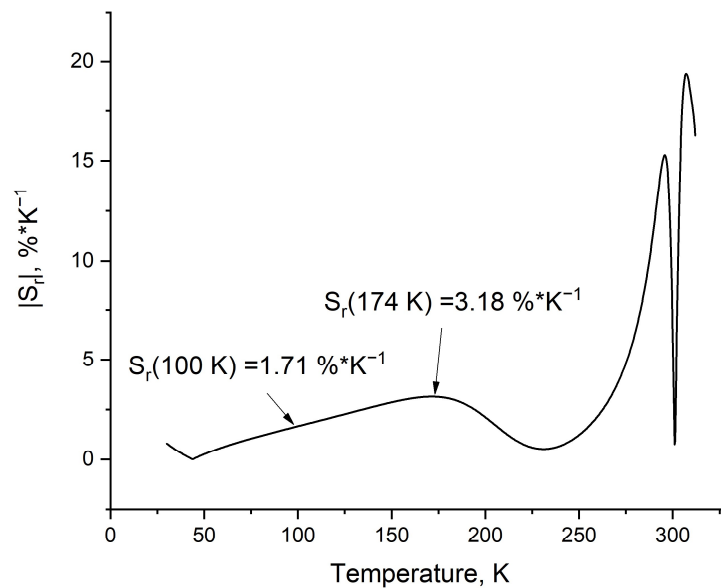
It can be seen that all luminescence intensity ratio (*LIR*) curves exhibit interesting behavior. Also, an important characteristic of temperature sensors is the absolute  $S_a$  and relative  $S_r$  temperature sensitivities (Figure 9a,b, respectively). We see that for the sample, we have obtained a competitive temperature sensitivity  $S_a$  in the 50–180 K temperature range. Note that the presence of the crank points is related to the use of absolute values of the  $S_a$  and  $S_r$  functions [41].

$$S_a = \left| \frac{d(LIR)}{dT} \right| \tag{4}$$

$$S_r = \frac{1}{LIR} \left| \frac{d(LIR)}{dT} \right| * 100\% \tag{5}$$



(a)



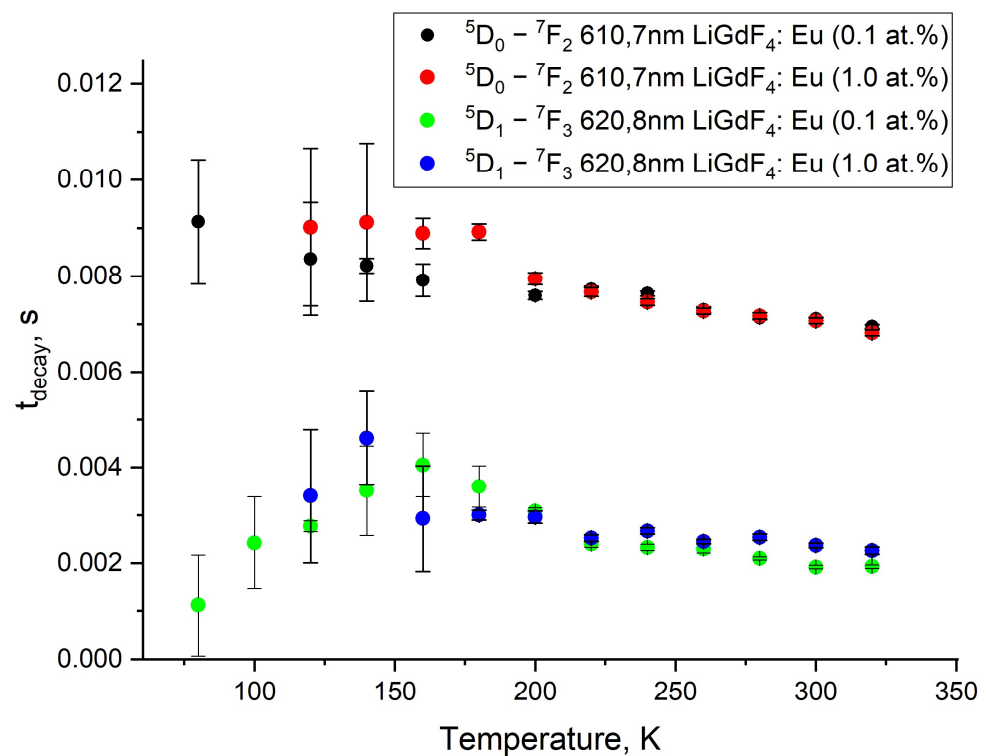
(b)

**Figure 9.** Absolute  $S_a$  (a) and relative  $S_r$  (b) temperature sensitivities of the  $\text{LiGdF}_4:\text{Eu}^{3+}$  (1 at.%) sample.

It can be seen from Figure 9b that the  $S_r$  reaches very competitive values. In particular,  $S_r$  has the first maximum at 174 K (3.18%/K). In its turn, at 100 K,  $S_r$  is equal to 1.71%/K. This value is quite competitive compared to such analogs as the  $\text{Er}^{3+}$ ,  $\text{Yb}^{3+}$ :  $\text{LaF}_3$  (~0.9%/K at 100 K) and  $\text{Pr}^{3+}$ ,  $\text{Yb}^{3+}$ :  $\text{LaF}_3$  (gradually decreases from ~1.0 at 30 K to ~0.2 at 100 K) cryogenic temperature sensors [16]. The same principle was used in [42], where, in  $\text{YVO}_4:\text{Eu}^{3+}$ , the LIR was based on the ratio of the  $\text{YVO}_4$  host and  $\text{Eu}^{3+}$  emission. In this system, the maximum  $S_r$  is ~4.0%/K at 123 K; however, in the 170–320 K range, the  $S_r$  values are in the 2.0–1.0%/K range, unlike the studied system.

### 3.4. Kinetic Characterization of the $\text{LiGd}_x\text{Y}_{1-x}\text{F}_4$ Samples at Room Temperature

The luminescence decay and rise curves of  $\text{Eu}^{3+}$  are very important kinetic characteristics of the phosphors. Indeed, there is a huge class of luminescence temperature sensors based on the analysis of the temperature-dependent kinetic characteristics of the luminescence signal [27,41,43–46]. For the studied  $\text{LiGdF}_4:\text{Eu}^{3+}$  (0.1 and 1.0 at.%) samples, there is a series of intense peaks in the red spectral part corresponding to the radiative transitions from  $^5\text{D}_1$  and  $^5\text{D}_0$  levels of  $\text{Eu}^{3+}$  to their lower ones. The decay and rise times of the suitable transitions at different temperatures are represented in Figure 10a and b, respectively. The decay and rise curves are represented in Figure S5 (Supplementary Materials). Such a significant difference in the kinetics of the rise and decay curves occurs due to the cross-relaxation between  $\text{Eu}^{3+}$  ions. Such a notable difference in the kinetics of the rise and decay of luminescence occurs due to the processes of cross-relaxation between  $\text{Eu}^{3+}$  ions.



(a)

Figure 10. Cont.

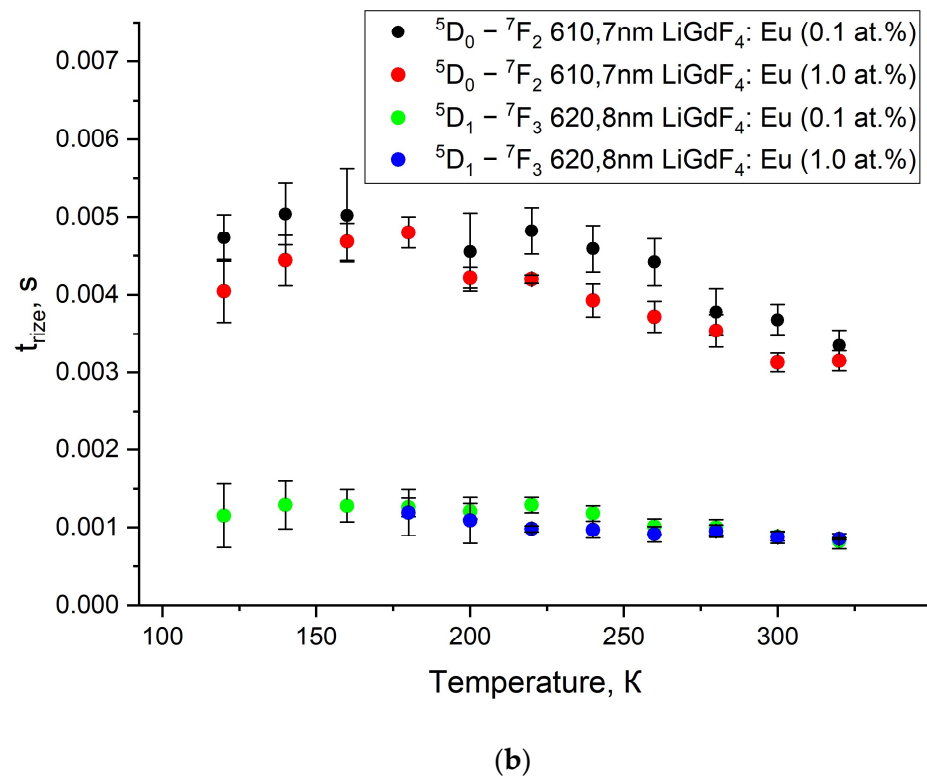


**Figure 10.** Luminescence decay (a) and rise (b) times of  $\text{LiGdF}_4:\text{Eu}^{3+}$  (0.1 and 1.0 at.%) at 610.7 ( ${}^5D_0$  emission) and 620.8 nm ( ${}^5D_1$  emission) in the 80–320 K temperature range.

It can be seen from Figure 10b that the decay times for the  ${}^5D_1$  and  ${}^5D_0$  states are around 7 and 3 ms at 300 K, respectively. The obtained results are in good agreement with the literature data on  $\text{LiGdF}_4$  [47,48]. The decay times demonstrate a weak tendency to decrease with an increase in temperature. This tendency can be attributed to the increase in the probability of non-radiative relaxation with the rise in temperature. The presence of the rise-time curve is explained by non-radiative relaxation from the higher-energy  ${}^5D_1$  levels to  ${}^5D_{1,0}$  ones (the excitation of  ${}^5D_{1,0}$  state is non-resonant). When the temperature is lowered, relaxation rates slow down, which is indicated by an increase in the rise-time [47]. Based on Figures 8 and 9 in the  $\text{LiGdF}_4:\text{Eu}^{3+}$  samples, it was found that the cross-relaxation process weakly depends on the temperature and concentration of  $\text{Eu}^{3+}$  ions and is not suitable for sensing purposes. The same tendency is observed in such important fluoride phosphors as  $\text{K}_2\text{Li}_2\text{La}_{1-x}\text{Eu}_x\text{F}_{10}$  in the 80–300 K range. Specifically, the  ${}^5D_1$  lifetime decreases gradually from  $\sim 4$  (80 K) to  $\sim 2$  ms (300 K) [49]. The rise times for the  ${}^5D_1$  and  ${}^5D_0$  states are around 1 and 3 ms at 300 K, respectively. The same values were obtained for  $\text{Eu}^{3+}:\text{LiGdF}_4$  in Ref. [47]. The rise times also demonstrate a decreasing tendency with the temperature increase.

#### 4. Conclusions

In this work, the physical characterization of  $\text{LiGd}_x\text{Y}_{1-x}\text{F}_4$  ( $x = 0.05; 0.3; 0.7$  and  $1.0$ ) and  $\text{LiGdF}_4:\text{Eu}^{3+}$  microparticles was carried out. The XRD method confirmed that all the samples have a tetragonal structure that corresponds to  $\text{LiYF}_4$  and  $\text{LiGdF}_4$  matrices. For the  $\text{LiGd}_x\text{Y}_{1-x}\text{F}_4$  ( $x = 0.05$ ) bulk crystal, the distribution coefficient was determined for the first time. It was equal to 0.84. Based on kinetic characterization data, the  $\text{LiGdF}_4$  sample was chosen for further  $\text{Eu}^{3+}$  doping (0.1 and 1.0 at.% concentrations). It was shown that for the  $\text{LiGdF}_4:\text{Eu}^{3+}$  (0.1%) sample, both  $\text{Gd}^{3+}$  and  $\text{Eu}^{3+}$  emissions were clearly observed under the excitation of  $\text{Gd}^{3+}$ . This fact indicates an efficient energy transfer from  $\text{Gd}^{3+}$  to  $\text{Eu}^{3+}$ . However, for the  $\text{LiGdF}_4:\text{Eu}^{3+}$  (1.0%) sample, the  $\text{Gd}^{3+}$  emission was negligible. In its turn, the intense  $\text{Eu}^{3+}$  emission was observed in the red part of the spectrum. These findings

make the  $\text{LiGdF}_4:\text{Eu}^{3+}$  material relevant for creating coatings of solar silicon cells in order to convert UV light into visible light. The temperature-dependent spectral characterization of the  $\text{LiGdF}_4:\text{Eu}^{3+}$  (1.0%) sample revealed that in the 30–250 K temperature range, a broad emission peak is evident. Its intensity sharply increases with the temperature decrease in the range of 30–150 K. We associated this phenomenon with the emission of defects, which is often found in fluorides and is associated with the formation of complexes of oxygen, fluorine vacancy, and RE. The integrated luminescence intensity ratio of this broad peak and  $\text{Eu}^{3+}$  emission was taken as a temperature-dependent parameter. The  $S_r$  reached very competitive values. In particular,  $S_r$  has the first maximum at 174 K (3.18%/K). In its turn, at 100 K,  $S_r$  is equal to 1.71%/K. The kinetic characteristics of both  $\text{Gd}^{3+}$  and  $\text{Eu}^{3+}$  did not demonstrate notable temperature dependence. Finally, it can be concluded that the  $\text{LiGdF}_4:\text{Eu}^{3+}$  showed a possibility of being used as an optical temperature sensor operating in the cryogenic temperature range. The next step forward concerning the present work is to develop the precise procedure of the separation of the luminescence signals of the broad emission and the doping ions. To control and estimate the amount of the defects, the development of the  $\text{LiGdF}_4$  synthesis procedure is also an important task. Finally, the interesting dependence of  $\text{Gd}^{3+}$  decay times on temperature will also be investigated.

**Supplementary Materials:** The following supporting information can be downloaded at: <https://www.mdpi.com/article/10.3390/ceramics7010018/s1>, Figure S1. The photo of the  $\text{Gd}^{3+}$  (5 at.%) $\text{LiYF}_4$  sample for the determination of the distribution coefficient; Table S1. Lattice parameters of  $\text{LiGd}_x\text{Y}_{1-x}\text{F}_4$ ; Figure S2. Absorption spectra of the  $\text{LiGd}_x\text{Y}_{1-x}\text{F}_4$  sample ( $x = 0.05$ ) at different distances from the crystal cap; Figure S3. Kinetics of luminescence of: (a)  $\text{LiGd}_x\text{Y}_{1-x}\text{F}_4$  ( $x = 0.05$ ), (b)  $\text{LiGd}_x\text{Y}_{1-x}\text{F}_4$  ( $x = 0.3$ ), (c)  $\text{LiGd}_x\text{Y}_{1-x}\text{F}_4$  ( $x = 0.7$ ) and (d)  $\text{LiGd}_x\text{Y}_{1-x}\text{F}_4$  ( $x = 1.0$ ) at the 312 nm; wavelength (6P7/2-8S7/2) at a temperature 100 K (black), 200 K (red), 300 K (blue); Figure S4. The pictures of both  $\text{LiGdF}_4:\text{Eu}^{3+}$  (0.1%) (a) and  $\text{LiYF}_4:\text{Eu}^{3+}$  (0.1%) (b) under 274 nm excitation; Figure S5. Kinetics of luminescence of  $\text{LiGdF}_4:\text{Eu}^{3+}$  (1 at.%) in the different wavelength: (a) kinetics of luminescence decay in the 610.7 nm, (b) kinetics of luminescence rise in the 610.7 nm, (c) kinetics of luminescence decay in the 620.8 nm and (d) kinetics of luminescence rise in the 620.8 nm at a temperature 160 K (black), 240 K (red), 320 K (green).

**Author Contributions:** E.I.O.: methodology, data curation, investigation, writing—original draft preparation; O.A.M.: methodology, data curation, investigation, writing—original draft preparation; S.L.K.: methodology, investigation; M.S.P.: conceptualization, methodology, data curation, investigation, writing—original draft preparation, project administration, funding acquisition. All authors have read and agreed to the published version of the manuscript.

**Funding:** Physical characterization and optical spectroscopy experiments were funded by the subsidy allocated to Kazan Federal University for the state assignment in the sphere of scientific activities (project number FZSM-2022-0021). Crystal growth procedures were funded by the Russian Science Foundation Grant No. 22-12-00259.

**Institutional Review Board Statement:** Not applicable.

**Informed Consent Statement:** Not applicable.

**Data Availability Statement:** The data presented in this study are available in this article and supplementary material.

**Conflicts of Interest:** The authors declare no conflicts of interest.

## References

1. Morozov, O.A.; Korableva, S.L.; Pudovkin, M.S.; Shakirov, A.A.; Shavelev, A.A.; Cherosov, M.A.; Klimovitskii, A.E.  $\text{Pr}^{3+}:\text{LiGdF}_4$  microparticles for optical temperature sensing. *Solid State Commun.* **2022**, *351*, 114792. [CrossRef]
2. Lepoutre, S.; Boyer, D.; Mahiou, R. Quantum cutting abilities of sol-gel derived  $\text{LiGdF}_4:\text{Eu}^{3+}$  powders. *J. Lumin.* **2008**, *128*, 635–641. [CrossRef]
3. Velázquez, J.J.; Mosa, J.; Gorni, G.; Balda, R.; Fernández, J.; Pascual, L.; Castro, Y. Transparent  $\text{SiO}_2\text{-GdF}_3$  sol-gel nano-glass ceramics for optical applications. *J. Sol-Gel Sci. Technol.* **2019**, *89*, 322–332. [CrossRef]
4. Wegh, R.T.; Donker, H.; Oskam, K.D.; Meijerink, A. Visible quantum cutting in  $\text{LiGdF}_4:\text{Eu}^{3+}$  through downconversion. *Science* **1999**, *283*, 663–666. [CrossRef]

5. Choi, J.E.; Kim, H.K.; Kim, Y.; Kim, G.; Lee, T.S.; Kim, S.; Jang, H.S. 800 nm near-infrared light-excitable intense green-emitting Li(Gd,Y)F<sub>4</sub>:Yb, Er-based core/shell/shell upconversion nanophosphors for efficient liver cancer cell imaging. *Mater. Des.* **2020**, *195*, 108941. [[CrossRef](#)]
6. Shin, J.; Kyhm, J.H.; Hong, A.R.; Song, J.D.; Lee, K.; Ko, H.; Jang, H.S. Multicolor tunable upconversion luminescence from sensitized seed-mediated grown LiGdF<sub>4</sub>: Yb, Tm-based core/triple-shell nanophosphors for transparent displays. *Chem. Mater.* **2018**, *30*, 8457–8464. [[CrossRef](#)]
7. Morozov, O.A.; Korableva, S.L.; Nurtdinova, L.A.; Kyashkin, V.M.; Popov, P.A.; Klimovitskii, A.E.; Semashko, V.V. Growth and characterization of optical and thermal properties of LiGdF<sub>4</sub> single crystal. *Opt. Mater.* **2023**, *137*, 113490. [[CrossRef](#)]
8. Lepoutre, S.; Boyer, D.; Mahiou, R. Structural and optical characterizations of sol-gel based fluorides materials: LiGdF<sub>4</sub>:Eu<sup>3+</sup> and LiYF<sub>4</sub>:Er<sup>3+</sup>. *Opt. Mater.* **2006**, *28*, 592–596. [[CrossRef](#)]
9. Yu, F.; Ma, B.; Xie, Z.; Wang, P.; Wu, X.; Lin, C.; Zhang, Q. Developing “smart windows” for optical storage and temperature sensing based on KNN transparent ceramics. *J. Eur. Ceram. Soc.* **2023**, *43*, 4408–4418. [[CrossRef](#)]
10. Aseev, V.; Babkina, A.; Evstropiev, S.; Kuzmenko, N.; Sevastianova, I.; Prokuratov, D.; Khodasevich, M. Structural and Luminescence Properties of (Gd<sub>1-x</sub>Y<sub>x</sub>)<sub>2</sub>O<sub>3</sub> Powders Doped with Nd<sup>3+</sup> Ions for Temperature Measurements. *Ceramics* **2022**, *5*, 1185–1197. [[CrossRef](#)]
11. Mikhaylov, D.A.; Potanina, E.A.; Nokhrin, A.V.; Orlova, A.I.; Yunin, P.A.; Sakharov, N.V.; Tabachkova, N.Y. Investigation of the Microstructure of Fine-Grained YPO<sub>4</sub>: Gd Ceramics with Xenotime Structure after Xe Irradiation. *Ceramics* **2022**, *5*, 237–252. [[CrossRef](#)]
12. Shinde, V.V.; Kungatkar, R.G.; Dhoble, S.J. UVB-emitting Gd<sup>3+</sup>-activated M<sub>2</sub>O<sub>2</sub>S (where M = La, Y) for phototherapy lamp phosphors. *Luminescence* **2015**, *30*, 1257–1262. [[CrossRef](#)] [[PubMed](#)]
13. Shi, X.; Xue, Y.; Mao, Q.; Pei, L.; Li, X.; Liu, M.; Zhong, J. Eu<sup>3+</sup> single-doped phosphor with antithermal quenching behavior and multicolor-tunable properties for luminescence thermometry. *Inorg. Chem.* **2023**, *62*, 893–903. [[CrossRef](#)] [[PubMed](#)]
14. Na, H.; Jeong, J.S.; Chang, H.J.; Kim, H.Y.; Woo, K.; Lim, K.; Jang, H.S. Facile synthesis of intense green light emitting LiGdF<sub>4</sub>:Yb, Er-based upconversion bipyramidal nanocrystals and their polymer composites. *Nanoscale* **2014**, *6*, 7461–7468. [[CrossRef](#)]
15. Faria, W.J.; Gonçalves TD, S.; de Camargo, A.S. Near infrared optical thermometry in fluorophosphate glasses doped with Nd<sup>3+</sup> and Nd<sup>3+</sup>/Yb<sup>3+</sup>. *J. Alloys Compd.* **2021**, *883*, 160849. [[CrossRef](#)]
16. Kaczmarek, A.M.; Kaczmarek, M.K.; Van Deun, R. Er<sup>3+</sup>-to-Yb<sup>3+</sup> and Pr<sup>3+</sup>-to-Yb<sup>3+</sup> energy transfer for highly efficient near-infrared cryogenic optical temperature sensing. *Nanoscale* **2019**, *11*, 833–837. [[CrossRef](#)]
17. Xia, W.; Li, L.; Yang, P.; Ling, F.; Wang, Y.; Cao, Z.; Hua, Y. Synthesis of color-tunable Sr<sub>8</sub>MgLa(PO<sub>4</sub>)<sub>7</sub>: Eu<sup>3+</sup>/Tb<sup>3+</sup> phosphors for designing dual-model thermometers. *J. Lumin.* **2021**, *239*, 118383. [[CrossRef](#)]
18. Trannoy, V.; Carneiro Neto, A.N.; Brites, C.D.; Carlos, L.D.; Serier-Brault, H. Engineering of mixed Eu<sup>3+</sup>/Tb<sup>3+</sup> metal-organic frameworks luminescent thermometers with tunable sensitivity. *Adv. Opt. Mater.* **2021**, *9*, 2001938. [[CrossRef](#)]
19. Nizamutdinov, A.S.; Kuznetsov, S.V.; Madirov, E.I.; Voronov, V.V.; Khadiev, A.R.; Yapyrintsev, A.D.; Ivanov, V.K.; Semashko, V.V.; Fedorov, P.P. Down-conversion luminescence of Yb<sup>3+</sup> in novel Ba<sub>4</sub>Y<sub>3</sub>F<sub>17</sub>:Yb:Ce solid solution by excitation of Ce<sup>3+</sup> in UV spectral range. *Opt. Mater.* **2020**, *108*, 110185. [[CrossRef](#)]
20. Zhai, X.; Lei, P.; Zhang, P.; Wang, Z.; Song, S.; Xu, X.; Zhang, H. Growth of lanthanide-doped LiGdF<sub>4</sub> nanoparticles induced by LiLuF<sub>4</sub> core as tri-modal imaging bioprobes. *Biomaterials* **2015**, *65*, 115–123. [[CrossRef](#)] [[PubMed](#)]
21. Grzechnik, A.; Crichton, W.A.; Bouvier, P.; Dmitriev, V.; Weber, H.P.; Gesland, J.Y. Decomposition of LiGdF<sub>4</sub> scheelite at high pressures. *J. Phys. Condens. Matter* **2004**, *16*, 7779. [[CrossRef](#)]
22. Yin, J.; Zhang, Q.; Liu, T.; Song, M.; Wang, X.; Zhang, H. Ab initio lattice relaxation and electronic structures of LiYF<sub>4</sub> crystals containing VF color center. *Phys. B Condens. Matter* **2009**, *404*, 1053–1057. [[CrossRef](#)]
23. Xiong, J.; Peng, H.; Hu, P.; Hang, Y.; Zhang, L. Optical characterization of Tm<sup>3+</sup> in LiYF<sub>4</sub> and LiLuF<sub>4</sub> crystals. *J. Phys. D Appl. Phys.* **2010**, *43*, 185402. [[CrossRef](#)]
24. Gulliver, G.H. The Quantitative Effect of Rapid Cooling Upon the Constitution of Binary Alloys. *J. Inst. Met.* **1913**, *9*, 120–157.
25. Mayerhöfer, T.G.; Pipa, A.V.; Popp, J. Beer’s law-why integrated absorbance depends linearly on concentration. *ChemPhysChem* **2019**, *20*, 2748–2753. [[CrossRef](#)] [[PubMed](#)]
26. De Vries, A.J.; Hazenkamp, M.F.; Blasse, G. On the Gd<sup>3+</sup> luminescence and energy migration in Li(Y,Gd)F<sub>4</sub>–Tb<sup>3+</sup>. *J. Lumin.* **1988**, *42*, 275–282. [[CrossRef](#)]
27. Pudovkin, M.S.; Ginkel, A.K.; Morozov, O.A.; Kiiamov, A.G.; Kuznetsov, M.D. Highly-sensitive lifetime optical thermometers based on Nd<sup>3+</sup>, Yb<sup>3+</sup>:YF<sub>3</sub> phosphors. *J. Lumin.* **2022**, *249*, 119037. [[CrossRef](#)]
28. Feldmann, C.; Jüstel, T.; Ronda, C.R.; Wiechert, D.U. Quantum efficiency of down-conversion phosphor LiGdF<sub>4</sub>: Eu. *J. Lumin.* **2001**, *92*, 245–254. [[CrossRef](#)]
29. Sun, Y.; Zou, H.; Zhang, B.; Zhou, X.; Song, Y.; Zheng, K.; Sheng, Y. Luminescent properties and energy transfer of Gd<sup>3+</sup>/Eu<sup>3+</sup> co-doped cubic CaCO<sub>3</sub>. *J. Lumin.* **2016**, *178*, 307–313. [[CrossRef](#)]
30. Reid, M.F.; Van Pieterse, L.; Wegh, R.T.; Meijerink, A. Spectroscopy and calculations for 4f<sup>N</sup> → 4f<sup>N-1</sup>5d transitions of lanthanide ions in LiYF<sub>4</sub>. *Phys. Rev. B* **2000**, *62*, 14744. [[CrossRef](#)]
31. Lo, D.; Makhov, V.N.; Khaidukov, N.M.; Krupa, J.C. Two-photon excitation to 4f65d configuration of Gd<sup>3+</sup> in LiGdF<sub>4</sub> crystal by KrF excimer laser. *J. Lumin.* **2006**, *119*, 28–32. [[CrossRef](#)]

32. Niranjana, V.; Janani, K.; Darba, V.R.; Ramasubramanian, S. Investigations on the synthesis dependent luminescence property of  $\text{LiGdF}_4:\text{Eu}^{3+}$  microcrystals. *Optik* **2019**, *198*, 163233.
33. Donega, C.D.M.; Meijerink, A.; Blasse, G. Non-radiative relaxation processes of the  $\text{Pr}^{3+}$  ion in solids. *J. Phys. Chem. Solids* **1995**, *56*, 673–685. [[CrossRef](#)]
34. Zhang, Y.X.; Wang, S.X.; Di Alberto, L.; Yu, G.L.; Yu, H.H.; Zhang, H.J.; Wang, J.Y. Temperature-dependent fluorescence properties and diode-pumped deep red laser performance of Pr:  $\text{LiGdF}_4$  crystal. *Chin. Phys. Lett.* **2015**, *32*, 054210. [[CrossRef](#)]
35. Sheoran, S.; Singh, V.; Singh, S.; Kadyan, S.; Singh, J.; Singh, D. Down-conversion characteristics of  $\text{Eu}^{3+}$  doped  $\text{M}_2\text{Y}_2\text{Si}_2\text{O}_9$  (M = Ba, Ca, Mg and Sr) nanomaterials for innovative solar panels. *Prog. Nat. Sci. Mater. Int.* **2019**, *29*, 457–465. [[CrossRef](#)]
36. Pudovkin, M.S.; Ginkel, A.K.; Lukinova, E.V. Temperature sensitivity of  $\text{Nd}^{3+}$ ,  $\text{Yb}^{3+}:\text{YF}_3$  ratiometric luminescent thermometers at different  $\text{Yb}^{3+}$  concentration. *Opt. Mater.* **2021**, *119*, 111328. [[CrossRef](#)]
37. Hayes, W.; Yamaga, M.; Robbins, D.J.; Cockayne, B. Optical detection of excitation EPR in  $\text{LiYF}_4$ . *J. Phys. C Solid State Phys.* **1980**, *13*, L1011. [[CrossRef](#)]
38. Belsky, A.N.; Chevallier, P.; Gesland, J.Y.; Kirikova, N.Y.; Krupa, J.C.; Makhov, V.N.; Queffelec, M. Emission properties of  $\text{Nd}^{3+}$  in several fluoride crystals. *J. Lumin.* **1997**, *72*, 146–148. [[CrossRef](#)]
39. Meijer, J.M.; Aarts, L.; van der Ende, B.M.; Vlugt, T.J.; Meijerink, A. Downconversion for solar cells in  $\text{YF}_3:\text{Nd}^{3+}$ ,  $\text{Yb}^{3+}$ . *Phys. Rev. B* **2010**, *81*, 035107. [[CrossRef](#)]
40. Santos, H.D.A.; Novais, S.M.V.; Jacinto, C. Optimizing the Nd:YF<sub>3</sub> phosphor by impurities control in the synthesis procedure. *J. Lumin.* **2018**, *201*, 156–162. [[CrossRef](#)]
41. Dramićanin, M.D. Trends in luminescence thermometry. *J. Appl. Phys.* **2020**, *128*, 040902. [[CrossRef](#)]
42. Kolesnikov, I.E.; Mamonova, D.V.; Kurochkin, M.A.; Kolesnikov, E.Y.; Lahderanta, E. Optical thermometry by monitoring dual emissions from  $\text{YVO}_4$  and  $\text{Eu}^{3+}$  in  $\text{YVO}_4:\text{Eu}^{3+}$  nanoparticles. *ACS Appl. Nano Mater.* **2021**, *4*, 1959–1966. [[CrossRef](#)]
43. Dramićanin, M.D.; Antić, Ž.; Čulubrk, S.; Ahrenkiel, S.P.; Nedeljković, J.M. Self-referenced luminescence thermometry with  $\text{Sm}^{3+}$  doped  $\text{TiO}_2$  nanoparticles. *Nanotechnology* **2014**, *25*, 485501. [[CrossRef](#)]
44. Fu, Y.; Zhao, L.; Guo, Y.; Yu, H. Up-conversion luminescence lifetime thermometry based on the  $^1\text{G}_4$  state of  $\text{Tm}^{3+}$  modulated by cross relaxation processes. *Dalton Trans.* **2019**, *48*, 16034–16040. [[CrossRef](#)] [[PubMed](#)]
45. Maciejewska, K.; Bednarkiewicz, A.; Marciniak, L. NIR luminescence lifetime nanothermometry based on phonon assisted  $\text{Yb}^{3+}-\text{Nd}^{3+}$  energy transfer. *Nanoscale Adv.* **2021**, *3*, 4918–4925. [[CrossRef](#)] [[PubMed](#)]
46. Siai, A.; Haro-González, P.; Naifer, K.H.; Férid, M. Optical temperature sensing of  $\text{Er}^{3+}/\text{Yb}^{3+}$  doped  $\text{LaGdO}_3$  based on fluorescence intensity ratio and lifetime thermometry. *Opt. Mater.* **2018**, *76*, 34–41. [[CrossRef](#)]
47. Vergeer, P.; van Den Pol, E.; Meijerink, A. Time and temperature dependence of the emissions from the quantum-cutting phosphor  $\text{LiGdF}_4:\text{Eu}^{3+}$ . *J. Lumin.* **2006**, *121*, 456–464. [[CrossRef](#)]
48. Takeuchi, N.; Ishida, S.; Matsumura, A.; Ishikawa, Y.I. Time-Resolved Study of Luminescence in  $\text{LiGd}_{1-x}\text{F}_4:\text{Eu}^{3+}_x$ . *J. Phys. Chem. B* **2004**, *108*, 12397–12403. [[CrossRef](#)]
49. Solarz, P.; Ryba-Romanowski, W. Effect of temperature and activator concentration on relaxation of excited states of  $\text{Eu}^{3+}$  in  $\text{K}_5\text{Li}_2\text{La}_{1-x}\text{Eu}_x\text{F}_{10}$  crystals. *J. Phys. Chem. Solids* **2003**, *64*, 1289–1296. [[CrossRef](#)]

**Disclaimer/Publisher’s Note:** The statements, opinions and data contained in all publications are solely those of the individual author(s) and contributor(s) and not of MDPI and/or the editor(s). MDPI and/or the editor(s) disclaim responsibility for any injury to people or property resulting from any ideas, methods, instructions or products referred to in the content.